

# Recent experiments in trapped-ion quantum information processing at NIST

J. Chiaverini, M. D. Barrett, R. B. Blakestad, J. Britton, W. Itano, J. D. Jost,  
E. Knill, C. Langer, D. Leibfried, R. Ozeri, T. Schaetz, and D. J. Wineland

National Institute of Standards and Technology, Boulder, Colorado 80305, USA

## ABSTRACT

Atomic ions confined in segmented trap arrays provide a system for quantum information processing. We report on the execution of two simple quantum algorithms, quantum error correction and the quantum Fourier transform, using this implementation. The demonstration of these algorithms in a scalable system is one step towards the execution of useful, large-scale quantum algorithms.

**Keywords:** Atomic physics, Quantum algorithms, Quantum communication, Quantum computing, Quantum error correction, Quantum Fourier transform, Quantum information processing, Trapped ions

## 1. INTRODUCTION

Quantum information processing (QIP) will enable great efficiency gains in certain tasks, such as the factorization of large composite numbers,<sup>1</sup> when compared to classical information processing. The desired implementation of quantum algorithms in physical systems has spurred much experimental work examining candidate systems. Individual atomic ions confined in an electromagnetic trap and addressed with laser beams<sup>2</sup> show particular promise as a scalable system for QIP. The ions' internal hyperfine states have long coherence times<sup>3-6</sup> and hence are useful as the system's qubits (quantum two-level systems), while the coupled motion of the ions in the trap provides a means to perform multi-qubit entangling gates.<sup>7,8</sup> Manipulation of the ions' quantum states is performed by means of laser pulses, and ions can be shuttled between zones of a trap-array structure separately or in groups, providing one method for interaction of qubits in different parts of the array.<sup>9,10</sup>

At NIST, we use such a system to perform simple quantum algorithms with a few ions. A key strength of the trapped-ion approach is the ability to perform operations on a subset of the qubits dependent upon measurement outcomes of other qubits in real time, before the quantum information succumbs to decoherence. Here we describe the physical implementation of our ion quantum processor, including methods of manipulation of quantum information and the apparatus used to control the ion qubits. We report on the execution of a quantum-error-correcting protocol, a requirement for any implementation of large-scale QIP, and we will also describe the demonstration of the semiclassical Fourier transform in our scalable system. The latter algorithm is a key step in Shor's quantum factoring algorithm,<sup>1</sup> one of the most anticipated of the quantum protocols currently proposed.

## 2. COHERENT QUBIT MANIPULATION

In the experiments, we use  ${}^9\text{Be}^+$  ions confined to the axis of a multizone linear radio frequency Paul trap. The qubits comprise the electronic ground-state hyperfine levels  $|F = 1, m_F = -1\rangle$  and  $|F = 2, m_F = -2\rangle$  (denoted as  $|\uparrow\rangle$  or  $|0\rangle$  and  $|\downarrow\rangle$  or  $|1\rangle$  respectively, by analogy to the states of a spin- $\frac{1}{2}$  particle). The qubit levels are separated in frequency by approximately 1.28 GHz.

Measurement is accomplished through projection of the state of each qubit using state-dependent resonance fluorescence (an ion in the  $|\downarrow\rangle$  state fluoresces, while an ion in the  $|\uparrow\rangle$  state does not). Individual ion detections can be performed separately.<sup>11,12</sup>

---

Further author information: (Send correspondence to J.C.)

J.C.: E-mail: john.chiaverini@boulder.nist.gov

M.D.B.: Current address: Physics Department, University of Otago, Dunedin, New Zealand

T.S.: Current address: Max Planck Institut für Quantenoptik, Garching, Germany

## 2.1. Single-qubit rotations

Rotations corresponding to the operator  $R(\theta, \phi) = \cos(\theta/2) I - i \sin(\theta/2) \cos \phi \sigma_x - i \sin(\theta/2) \sin \phi \sigma_y$ , are realized with two-photon stimulated-Raman transitions<sup>9,13,14</sup> implemented by two laser beams having a relative frequency detuning equal to the qubit transition frequency. Here  $\sigma_x$  and  $\sigma_y$  are the usual Pauli operators,  $I$  is the identity operator,  $\theta$  is the rotation angle, and  $\phi$  is the angle of the rotation axis in the  $x$ - $y$  plane. Rotations around an axis  $A$  by an angle  $\theta$  will be denoted  $A_\theta$ , *e.g.*,  $X_{\pi/2} = R(\pi/2, 0)$ , although for rotations around an axis by  $\pi$  we will omit the angle subscript, *e.g.*,  $X = R(\pi, 0)$ .

## 2.2. Multi-qubit entangling operations

Implementation of the error-correcting code implemented here (described below) requires the creation of a three-qubit entangled state. Here, three qubits are entangled with a phase gate  $G$ , an extension of those described previously<sup>8,15</sup> utilizing the ions' quantized axial vibrational modes:

$$G(s_1, s_2, s_3) = G^{-1}(s_1, s_2, s_3) = \begin{cases} 1 & \text{if } s_1 = s_2 = s_3 \\ -1 & \text{otherwise.} \end{cases} \quad (1)$$

Here  $s_i \in \{\uparrow, \downarrow\}$  is the spin state of the  $i$ th ion. This operation is diagonal in the measurement basis. A “walking wave” polarization interference pattern is set up at the ions' location using two perpendicular beams of radiation whose wavevector difference is parallel to the trap axis and whose difference frequency is detuned by a small amount  $\delta$  ( $\approx 2\pi \times 70$  kHz) from the frequency  $\omega_{\text{COM}}$  ( $= 2\pi \times 3.7$  MHz) of the center-of-mass (COM) axial vibrational mode in the trap.<sup>8,14</sup> The inter-ion spacing is adjusted relative to the beams' interference pattern so that if the phase of the resulting oscillating optical-dipole force at frequency  $\omega_{\text{COM}} - \delta$  at the primary ion is  $\phi_P$ , the phases at the ancillae ions are  $\phi_{A1} = \phi_P + \frac{2\pi}{3}$  and  $\phi_{A2} = \phi_P + \frac{4\pi}{3}$ . The axial COM mode will be (off-resonantly) excited only if there is a net force on the ions, which is the case if the ions are in different internal states, *i.e.*, for all states except  $|\uparrow\uparrow\uparrow\rangle$  and  $|\downarrow\downarrow\downarrow\rangle$ . As the vibrational mode is excited, the ions move along a closed path in phase space (if the radiation is applied for a time equal to  $2\pi/\delta$ ), and the states acquire a phase proportional to the phase-space area enclosed by this path. All states except those for which  $s_1 = s_2 = s_3$  acquire the same phase (adjusted to be  $\pi$ ), since the magnitude of the net force on the ions is equal and nonzero.

The entangling gate required for the preparation of the approximate period 3 state as input to the semiclassical quantum Fourier transform demonstration (described below) creates a maximally entangled state of the outer two ions in a chain of three.<sup>11</sup> This operation is similar to that just described, except that the dipole forces are detuned by an amount  $\delta$  from the second vibrational mode (the “stretch” mode) of the ions' axial motion ( $\omega_{\text{STR}} = 2\pi \times 6.4$  MHz), as opposed to the COM mode. The phase acquired is not dependent upon the motion of the center ion, as the center ion does not participate in this mode. The spacing of the ions is such that the phase of the oscillating-dipole force is equivalent at the outer two ions' locations. When these two ions are in different internal states, the stretch mode is excited, and these states obtain a phase (adjusted to be  $\pi$ ), whereas states in which the outer ions' internal states are the same are not excited and do not acquire a phase. It is these phases, conditional on the ions' internal states, that enable the creation of qubit entanglement.

## 3. APPARATUS

Positive atomic ions are confined to a segmented, multizone, linear Paul trap.<sup>16</sup> Ions are ponderomotively confined in the radial directions by means of an average potential due to a radio-frequency (RF) quadrupole potential.<sup>17</sup> Axial confinement is achieved through application of static electric potentials to segmented control electrodes. The trap used in this work is depicted in Fig. 1. This trap consists of two gold-coated alumina wafers with electrodes defined via laser-machining and metal electroplating, and is similar in construction to a trap described previously.<sup>18</sup> The electrodes on the two wafers realize the quadrupolar configuration of a linear trap. The trap has six trapping zones, and ions can be moved between these zones, individually or in groups, through synchronized variation of the static potentials applied to the electrode segments.

There are both an ion-loading region, with a larger capture volume, and an experimental region, with tighter confinement for faster ion movement. The experimental region contains one narrow electrode defining a separation

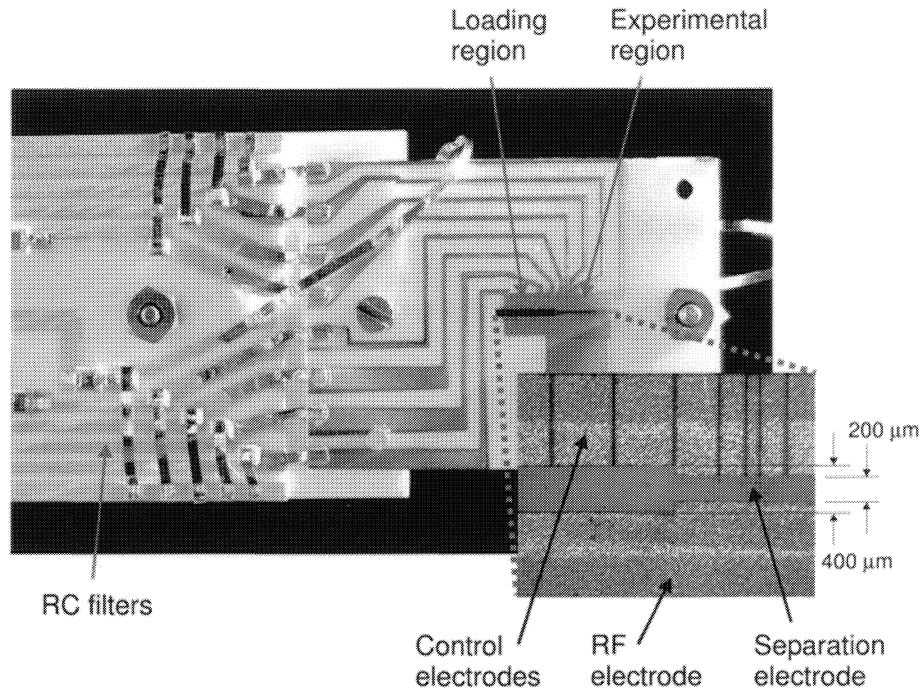


**Figure 1.** Picture of multizone ion trap used in this work. The electrodes are gold deposited on two insulating alumina wafers separated by an alumina spacer (only one of these alumina wafers can be seen in this figure). These wafers are attached to another alumina wafer containing leads and one stage of RC filters for the control electrodes. The inset shows a detail of the trapping region and electrodes.

zone, in which groups of ions may be separated into subgroups or individual ions. Separations of individual ions from groups for individual operations and measurement are performed in this zone. The shortest distance between an electrode and the trap axis in this structure is  $140 \mu\text{m}$ .

One stage of low-pass RC filtering for the control electrodes is implemented by means of surface-mount components mounted on a separate alumina board that is attached to the trap wafers. The trap and filters are mounted in a quarter-wave coaxial resonator that is used to produce an RF potential of approximately 200 V in amplitude at approximately 150 MHz. The trap is housed in a vacuum system having a typical pressure of approximately  $1 \times 10^{-11}$  Torr.

The frequencies of laser beams for cooling, manipulation, and detection are controlled using acousto- and electro-optic modulation, and the beams are admitted through windows surrounding the trap. Lasers are required for Doppler cooling and detection, optical pumping, and excitation of two-photon stimulated Raman transitions as described above. Ion fluorescence is detected by means of an F\1 imaging system and a photomultiplier tube. Beryllium atoms are produced by heating of a beryllium filament, and the atoms are ionized in the trapping region by accelerated electrons from a heated tungsten filament.

#### 4. QUANTUM ERROR CORRECTION

Both scalable quantum computation<sup>19</sup> and quantum communication require error control to protect quantum information against unavoidable noise. Quantum error correction<sup>20,21</sup> protects information stored in encoded qubits by rectifying errors with corrective operations conditioned on measurement outcomes. Experiments<sup>22-24</sup> using nuclear magnetic resonance have implemented error-correction protocols, but inherent limitations of the technique<sup>25</sup> prevent its application to scalable quantum information processing.

We experimentally demonstrate quantum error correction using three beryllium atomic-ion qubits confined to a linear, multizone trap (a more detailed explanation can be found elsewhere<sup>26</sup>). An encoded one-qubit state

**Table 1.** Syndromes and correction operations for the quantum error-correcting code. The first column shows the state of the primary qubit before a correction is applied. The fourth column shows the correction required to recover the primary qubit initial state  $|\psi_0\rangle_P = \alpha|\uparrow\rangle_P + \beta|\downarrow\rangle_P$ .

Primary qubit before correction	Error	Ancillary syndrome	Correction operation
$\beta \uparrow\rangle_P + \alpha \downarrow\rangle_P$	no error	$ \uparrow\uparrow\rangle_A$	$X$
$\alpha \uparrow\rangle_P + \beta \downarrow\rangle_P$	ancilla 1 flipped	$ \uparrow\downarrow\rangle_A$	$I$
$\alpha \uparrow\rangle_P + \beta \downarrow\rangle_P$	ancilla 2 flipped	$ \downarrow\uparrow\rangle_A$	$I$
$\beta \uparrow\rangle_P - \alpha \downarrow\rangle_P$	primary qubit flipped	$ \downarrow\downarrow\rangle_A$	$Y$

is protected against spin-flip errors by means of a three-qubit quantum error-correcting code. We verify error correction by comparing the corrected final state to the uncorrected state and to the initial state. In principle, implementations such as this can maintain a quantum state by means of repeated error correction, an important step towards scalable fault-tolerant quantum computation using trapped ions.

We describe the implementation of a quantum error-correcting code (QECC) using three physical qubits, here denoted as the primary qubit and ancillae 1 and 2, to encode and protect one logical qubit from spin-flip errors (a  $\pi$  rotation around the  $x$  axis, in this case). We implement the QECC by (i) preparing the state of the primary qubit, (ii) encoding this state into the logical state of all three qubits through use of an entangling operation, (iii) applying an error rotation (that induces spin-flips upon measurement) to all three qubits, (iv) decoding the logical state to the primary qubit, (v) measuring the state of the ancillae, and finally (vi) applying correction operations to the primary qubit dependent upon the ancillae measurement outcome. The error correction is performed deterministically in every experiment.

In contrast to the standard repetition code,<sup>20,21,27</sup> the QECC described and implemented here (see Fig. 2a) can not be obtained by application of the superposition principle to a classical error-correction code. As an error-correction code, it will correct a spin-flip on any of the three qubits (as demonstrated here). Alternatively, it can instead be used to correct several other error sets.<sup>26</sup>

Ion preparation before each implementation of the QECC protocol consists of Doppler cooling, Raman side-band cooling of all three axial modes of vibration to the ground state, and optical pumping of the ions to the  $|\downarrow\downarrow\downarrow\rangle$  state.<sup>9,28</sup> Each experiment also requires the initialization of the primary physical qubit to a state  $|\psi_0\rangle_P = \alpha|\uparrow\rangle_P + \beta|\downarrow\rangle_P$  with the ancillae initialized to the state  $|\downarrow\downarrow\rangle_A$ . This is accomplished by momentarily increasing the spacings between the three ions and then applying a rotation that affects the ions differently due to their respective positions in the laser beam intensity profile. This operation requires only one laser pulse.<sup>9</sup> The state of the primary qubit is then encoded in the state of all three qubits using a three-ion entangling operation as described in Sec. 2.2 above. In the following discussion we assume perfect entangling operations.

After encoding, we apply an “error”  $\theta_e$ , a rotation  $X_{\theta_e}$ , to all qubits by means of a stimulated-Raman transition with all ions illuminated equally. With respect to later measurement, this error induces a spin-flip on each physical qubit with probability  $p(\theta_e) = \sin^2(\frac{\theta_e}{2})$ . The state is then decoded using the inverse of the encoding operation. The decoding effects a transformation such that afterwards, the four possible states of the ancillae in the measurement basis (the error syndromes) depend on the error that has occurred; for at most one qubit flipped, the state of the primary qubit before a correction operation is applied is shown in Table 1. For technical reasons, the algorithm was constructed such that an  $X$  operation is required if no error had occurred.<sup>26</sup>

After the decoding operation, the ions are spatially separated (see Fig. 2b), and the state of the ancillae is determined. The ions are then moved so that only the primary qubit ion is addressed. Depending on the ancillae measurement outcome, a correction operation ( $X$ ,  $Y$ , or  $I$ , see Table 1) is applied to the primary qubit. This qubit is then analyzed to determine the effectiveness of the protocol through repetition of the experiment. After initial cooling and preparation of the state  $|\downarrow\downarrow\downarrow\rangle$ , each experiment requires approximately 4 ms to perform.

In principle, this QECC works perfectly only when at most one qubit undergoes a spin-flip error. Because there is a chance that more than one qubit will flip due to the applied error, most input states cannot be corrected



to all orders in the error  $\theta_e$ , though they can be corrected such that an improvement in the fidelity over the uncorrected case is attainable for small errors. The fidelity of the corrected final state (as derivable from the action of the code in Fig. 2a) as a function of the error will be

$$\begin{aligned} F(\theta_e) &= 1 - |\alpha|^2 |\beta|^2 (2 - 3 \cos \theta_e + \cos^3 \theta_e) \\ &\approx 1 - \frac{3}{4} |\alpha|^2 |\beta|^2 \theta_e^4 + O(\theta_e^6). \end{aligned} \quad (2)$$

For small errors, the infidelity is quadratic in  $\theta_e^2$ , whereas it is linear in  $\theta_e^2$  for the uncorrected state. The fidelity reaches a maximum value of 1 for the cases where  $|\alpha|^2 |\beta|^2 = 0$ . The input states  $|\downarrow\rangle_P$  (where  $\alpha = 0, |\beta| = 1$ ) and  $|\uparrow\rangle_P$  (where  $|\alpha| = 1, \beta = 0$ ) can therefore be corrected to all orders in  $\theta_e$  for any error  $X_{\theta_e}$  with this protocol.

To isolate the basic behavior of the protocol from the technical errors present in the coherent operations required for its implementation, we apply the complete protocol (Fig. 2a) with and without application of the error-correction operations and compare the final state fidelities. Figure 3a shows the results for the input state  $|\downarrow\rangle_P$ . The data are consistent with the theoretical prediction that the state should be corrected for any error  $X_{\theta_e}$  by this QECC. The curves have nonzero infidelity for zero error angle  $\theta_e$  due to infidelity present in the operations of the protocol.

Figures 3b and c show similar data for the initial states  $\sqrt{0.10} |\uparrow\rangle_P - i\sqrt{0.90} |\downarrow\rangle_P$  and  $\sqrt{0.22} |\uparrow\rangle_P - i\sqrt{0.78} |\downarrow\rangle_P$ , respectively. As the input state gets closer to the equator of the Bloch sphere ( $|\alpha| \approx |\beta|$ ), the QECC is expected to perform worse (Equation 2). However, the infidelity of the corrected state should grow only quadratically in  $\theta_e^2$  for small errors as opposed to a linear growth for the uncorrected state. This behavior can be observed in the data, which in all cases show an improvement over the uncorrected state.

We also plot the observed rate of the ancillary syndromes for a particular input state in Fig. 3d to verify that our QECC protocol is correctly detecting errors. The rate  $\Gamma(|\uparrow\uparrow\rangle_A)$  of the syndrome corresponding to no error and the sum of the rates  $\Gamma(|\uparrow\downarrow\rangle_A) + \Gamma(|\downarrow\uparrow\rangle_A) + \Gamma(|\downarrow\downarrow\rangle_A)$  of the syndromes corresponding to one error are plotted separately. The rates of the syndromes vary in the predicted manner for increasing error, up to an offset due to imperfections in the operations that make up the protocol.

Although an improvement in fidelity over an uncorrected encoded qubit was observed, the QECC protocol as implemented here induced more infidelity for small errors than would be acquired in an unencoded qubit subject to the applied error. It should be noted, however, that for errors larger than  $\theta_e \approx 1$  radian, the corrected state had higher fidelity than an unencoded qubit undergoing the applied error for all states investigated, and the logical state was genuinely protected with this protocol. The degradation observed during the execution of the QECC is due in large part to the fidelity of the encoding and decoding gates ( $\sim 90\%$ ), and all operations must be improved to achieve fault-tolerance. In spite of these technical difficulties, the current experiment demonstrates the feasibility of quantum error correction in a scalable system with resettable ancillae. With improvements in fidelity, the execution of the QECC can be made a useful part of more complex quantum algorithms.

## 5. QUANTUM FOURIER TRANSFORM

Among quantum algorithms discovered up to this time, Shor's method for factoring large composite numbers<sup>1</sup> may be large-scale quantum information processing's most prominent application, as efficient factoring would render current cryptographic techniques based on large composite-numbers vulnerable to attack. A key component of this algorithm is an order-finding subroutine that requires application of the quantum discrete Fourier transform (QFT) to determine the period of a set of quantum amplitudes.<sup>1, 27, 29, 30</sup> In addition, the polynomial-time QFT is responsible for most of the known instances of exponential speedup over classical algorithms.

Relative phase information of the output state from the QFT is not required when it is applied as mentioned above; only the measured probability amplitudes of each state are used. This allows the replacement of the fully coherent QFT with the semiclassical, or "measured" QFT,<sup>31</sup> in which each qubit is measured in turn, and prescribed controlled phase rotations on the other qubits are conditioned on the classical measurement outcomes. This eliminates the need for entangling gates in the QFT protocol, which, for the trapped-ion implementation,

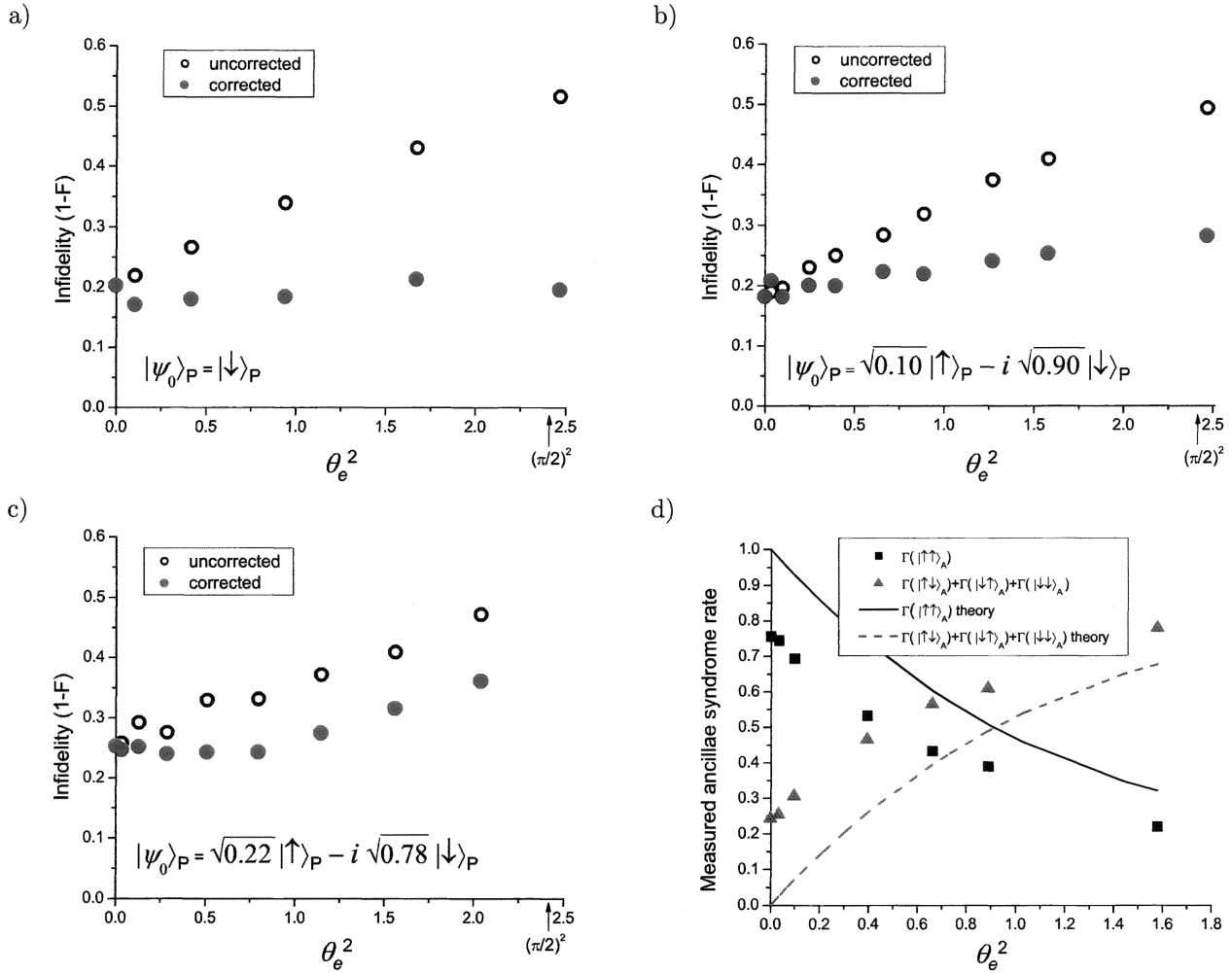


**Figure 3.** Results of quantum error correction protocol. Recovered state infidelity plotted versus square of the applied error for corrected and uncorrected cases for three initial states (a–c) and rate of syndrome measurements of ancillae (d). One-standard-deviation errors are approximately the size of the symbols. (a) The initial state is  $|\psi_0\rangle_P = |\downarrow\rangle_P$ . (b) The initial state is  $|\psi_0\rangle_P = \sqrt{0.10} |\uparrow\rangle_P - i\sqrt{0.90} |\downarrow\rangle_P$ . (c) The initial state is  $|\psi_0\rangle_P = \sqrt{0.22} |\uparrow\rangle_P - i\sqrt{0.78} |\downarrow\rangle_P$ . (d) Rate of syndrome measurements of ancillae versus square of error angle. The rate  $\Gamma(m)$  is the measured probability of obtaining the measurement outcome  $m$ . The data are offset from the theoretical curves because of imperfect gate operations. The initial state is  $|\psi_0\rangle_P = \sqrt{0.10} |\uparrow\rangle_P - i\sqrt{0.90} |\downarrow\rangle_P$  for these data.

**Table 2.** Periodic states prepared to test the semiclassical quantum Fourier transform protocol

Periodicity	State (normalization omitted)	Preparation fidelity
1	$ \psi_1\rangle =  000\rangle +  001\rangle +  010\rangle + \dots +  111\rangle$	0.98(1)
2	$ \psi_2\rangle =  001\rangle +  011\rangle +  101\rangle +  111\rangle$	0.98(1)
approx. 3	$ \psi_3\rangle =  011\rangle +  110\rangle +  001\rangle +  100\rangle$	0.90(2)
4	$ \psi_4\rangle =  011\rangle +  111\rangle$	0.98(1)
8	$ \psi_8\rangle =  111\rangle$	$> 0.99(1)$

considerably relaxes the required control of motional states. In addition, the semiclassical version is quadratically more efficient in the number of quantum gates when compared to the fully coherent version\*, a benefit in any physical implementation of quantum computing. The coherent QFT has been implemented in nuclear magnetic resonance systems<sup>32–36</sup> but has not been demonstrated in a scalable system.<sup>25</sup> Here we describe an implementation of the measured QFT in an architecture that can be scaled<sup>9,10</sup> (a more detailed explanation can be found elsewhere<sup>37</sup>).

The QFT is a basis transformation in an  $N$ -state space that transforms the state  $|k\rangle$  ( $k$  is an integer ranging from 0 to  $N - 1$ ) according to  $|k\rangle \rightarrow (1/\sqrt{N}) \sum_{j=0}^{N-1} e^{-i2\pi jk/N} |j\rangle$ . The action on an arbitrary superposition of states may be written as  $\sum_{k=0}^{N-1} x_k |k\rangle \rightarrow \sum_{j=0}^{N-1} y_j |j\rangle$ , where the complex amplitudes  $y_j$  are the discrete Fourier transform<sup>38</sup> of the complex amplitudes  $x_k$ . For three qubits, switching to binary notation, where  $k_1$ ,  $k_2$ , and  $k_3$  are the most to least significant bits in the label for the state  $|k_1 k_2 k_3\rangle = |k_1\rangle \otimes |k_2\rangle \otimes |k_3\rangle$  ( $k_i \in \{0, 1\}$ ), the transform can be written as<sup>27</sup>

$$|k_1 k_2 k_3\rangle \rightarrow \frac{1}{\sqrt{8}} \left( |0\rangle + e^{i2\pi[0.k_3]} |1\rangle \right) \otimes \left( |0\rangle + e^{i2\pi[0.k_2 k_3]} |1\rangle \right) \otimes \left( |0\rangle + e^{i2\pi[0.k_1 k_2 k_3]} |1\rangle \right), \quad (3)$$

where  $[0.q_1 q_2 \dots q_n]$  denotes the binary fraction  $q_1/2 + q_2/4 + \dots + q_n/2^n$ . When written in this form, it can be seen that the QFT is the application to each qubit of a Hadamard transformation and a  $z$  rotation conditioned on each of the less significant qubits followed by a bit-order reversal.<sup>27</sup> The three-qubit quantum circuit, without the bit-order reversal, is shown in Fig. 4a. The simplified circuit for the measured QFT is shown in Fig. 4b.

In the experiment,  $z$  rotations are transformed into  $x$  rotations, which are more straightforward to implement in our system, and rotations are redistributed to accommodate required spin-echo refocussing pulses ( $\pi$ -rotations) that reduce dephasing due to fluctuating magnetic fields,<sup>18,39,40</sup> but this does not change the basic protocol. We have applied this three-qubit QFT to input states of several different periodicities. The QFT protocol proceeded with ions located in the multi-zone trap as shown in Fig. 4c.

Five different states were prepared to test the QFT protocol (see Table 2). These states have periods of 1, 2, 4, 8, and approximately 3. The three-qubit state space consists of eight states, labeled  $|000\rangle$ ,  $|001\rangle$ ,  $\dots$ ,  $|111\rangle$  in binary notation and ordered lexicographically. The periodicity is derived from the recurrence of the quantum amplitudes in a superposition of these eight states. The state  $|\psi_3\rangle$  is only approximate, because there is no exact period 3 state in the eight-state space of three qubits. This state is a cyclical permutation of the four-component superposition state  $|000\rangle + |011\rangle + |110\rangle + |001\rangle$ , although the former is easier to prepare in our system.

For each input state, several thousand implementations of the QFT were performed, each involving: (i) rotation of ion 1, (ii) measurement of ion 1, (iii) rotation of ion 2 conditional on the measurement of ion 1, (iv) measurement of ion 2, (v) rotation of ion 3 conditional on the first two measurements, and (vi) measurement of ion 3. Each experiment required approximately 4 ms after initial cooling and state preparation.

The measured output state probabilities after application of the QFT algorithm are shown in Fig. 5 along with the theoretically expected probabilities for the five different input states. The data generally agree with the theoretical predictions, although the deviations from the predicted values are larger than can be explained

\*For  $n$  qubits, the number of quantum gates is  $O(n)$  rather than  $O(n^2)$ .

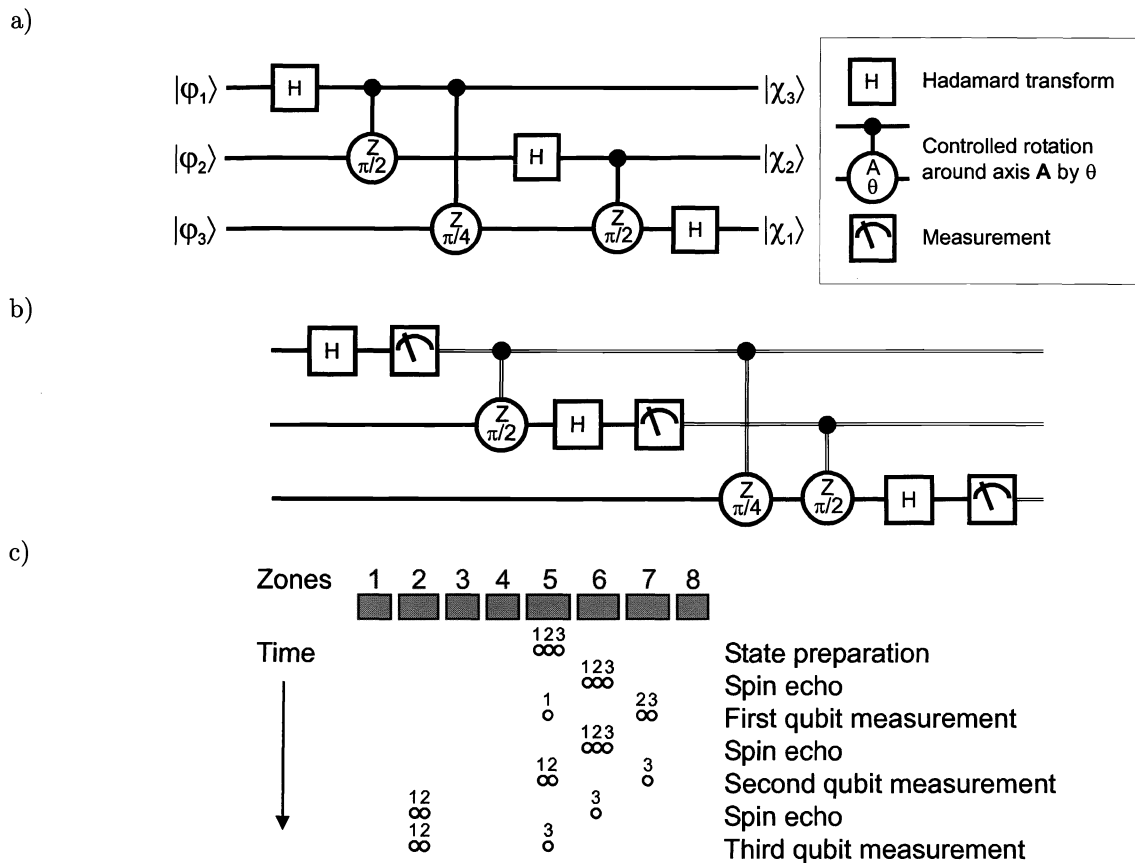


**Figure 4.** Circuits for the quantum Fourier transform (QFT) of three qubits. (a) The QFT as composed of Hadamard transforms and two-qubit conditional phase gates.<sup>27</sup> The  $|\varphi_i\rangle$  and  $|\chi_i\rangle$  are the input and output states, respectively, of qubit  $i$ . The most significant qubit corresponds to  $i = 1$ . This circuit produces the QFT in reverse bit order.<sup>27</sup> (b) The semiclassical (or “measured”) quantum Fourier transform.<sup>31</sup> The double lines denote classical information. This circuit can be implemented by means of a single classically-controlled quantum operation on each qubit. The protocol is preceded by state preparation (not shown) of the quantum state to be transformed. (c) Locations of the ions in the multizone trap during the semiclassical QFT execution as a function of time. Separation of ions and refocussing operations are performed in zone 6, and all other qubit operations are performed in zone 5.

statistically, and are due to systematic errors in the experiment. These systematic errors are associated with the state preparation (not associated with the QFT protocol) as well as with the separate detections and conditional rotations of the three ions (intrinsic to the QFT protocol). The first, second, and third ions were measured approximately 1.2 ms, 2.4 ms, and 3.5 ms after the beginning of the algorithm. Dephasing due to slow local magnetic field fluctuations, though mitigated by the refocussing (spin-echo) operations, grows as a function of time during each experiment; the chance that an error occurs due to dephasing grows from approximately 5 % for the first ion to approximately 13 % for the third ion.

Even with these systematic errors, the results compare well with theory, as can be shown by examining the squared statistical overlap (SSO) (derived from the statistical overlap defined elsewhere<sup>41</sup>) of each set of data with the associated predictions. Here we define the SSO as  $\gamma = \left( \sum_{j=0}^7 m_j^{\frac{1}{2}} e_j^{\frac{1}{2}} \right)^2$ , with the measured and expected output state probabilities of state  $j$  denoted  $m_j$  and  $e_j$ , respectively. This is an effective measure of fidelity without regard for relative output phases. The lowest SSO for the five prepared states is 0.87, suggesting that peaks can be reliably located to determine periodicities as required for Shor's factorization algorithm.

These results demonstrate that for small state-spaces, the QFT can be performed semiclassically with a signal-to-noise level sufficient for period-finding in quantum algorithms by means of a system of trapped-ion qubits. Even with input state infidelities as large as 0.10, as in the period 3 state created here, the measured QFT had significant squared statistical overlap with the theoretical prediction for the correct input state. Extension of the technique described here to larger quantum registers<sup>9,10</sup> is a function only of trap-array size and involves a linear overhead in ion separation and movement. The main source of intrinsic error in our implementation was qubit dephasing due to magnetic field fluctuations. Use of first-order magnetic-field-independent qubit transitions<sup>6,9</sup> can mitigate this problem and lead to a high-fidelity method for implementation of the QFT, a necessary step toward large-number-factorization applications of quantum computing.

## ACKNOWLEDGMENTS

The authors thank D. Hume and R. Reichle for helpful comments on the manuscript. This work was supported by the U. S. National Security Agency (NSA) and the Advanced Research and Development Activity (ARDA). This manuscript is a publication of NIST and is not subject to U. S. copyright.

## REFERENCES

1. P. W. Shor in *Proceedings of the 35th Annual Symposium on Foundations of Computer Science*. S. Goldwasser, ed. (IEEE Computer Society Press, Los Alamitos, CA, 1994), p. 124.
2. J. I. Cirac and P. Zoller, "Quantum computations with cold trapped ions," *Phys. Rev. Lett.* **74** 4091–4094 (1995).
3. J. J. Bollinger *et al.*, "A 303-MHz Frequency Standard Based on Trapped Be<sup>+</sup> Ions," *IEEE Trans. on Instrum. and Meas.* **40**, 126 (1991).
4. P. T. H. Fisk *et al.*, "Very high Q microwave spectroscopy on trapped <sup>171</sup>Yb<sup>+</sup> ions: application as a frequency standard," *IEEE Trans. on Instrum. and Meas.* **44**, 113 (1995).
5. C. F. Roos *et al.*, "Bell states of atoms with ultralong lifetimes and their tomographic state analysis," *Phys. Rev. Lett.* **92**, 220402 (2004).
6. C. Langer *et al.*, "Long-lived qubit memory using atomic ions," submitted for publication. arXiv e-print quant-ph/0504076.
7. F. Schmidt-Kaler *et al.*, "Realization of the CiracZoller controlled-NOT quantum gate," *Nature* **422**, 408–411, (2003).
8. D. Leibfried *et al.*, "Experimental demonstration of a robust, high-fidelity geometric two ion-qubit phase gate," *Nature* **422**, 412–415, (2003).
9. D. J. Wineland *et al.*, "Experimental issues in coherent quantum-state manipulation of trapped atomic ions," *J. Res. Natl. Inst. Stand. Technol.* **103** (3), 259–328 (1998).
10. D. Kielpinski, C. Monroe, D. J. Wineland, "Architecture for a Large-Scale Ion-Trap Quantum Computer," *Nature* **417**, 709 (2002).

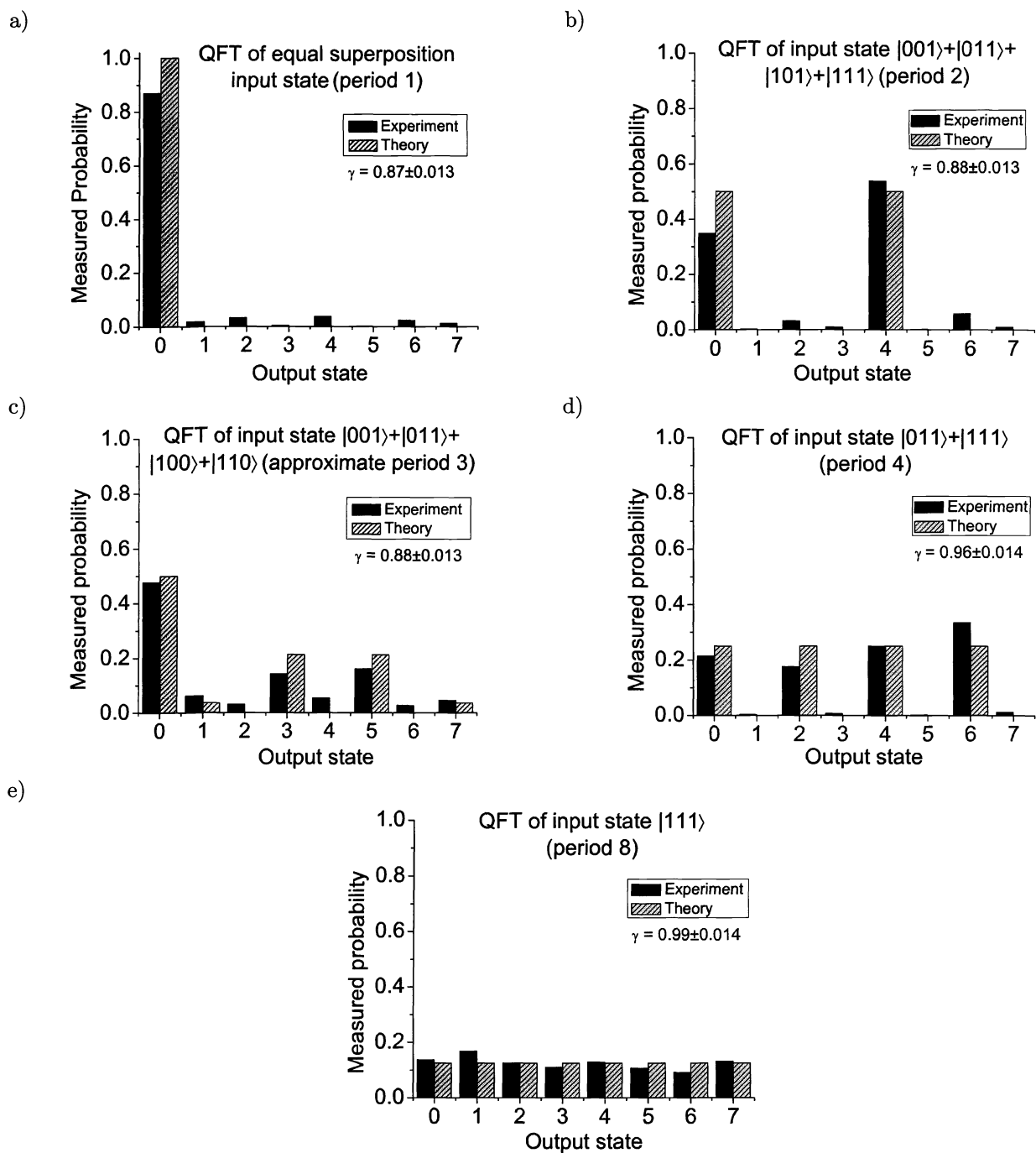


**Figure 5.** Results of the semiclassical quantum Fourier transform. Measured probability of each output state occurring after the application of the protocol is shown along with the expected transform output. Each plot contains data from 5000 experiments. The squared statistical overlap (SSO)  $\gamma$ , a measure of transform accuracy, is explained in the text. Uncertainties quoted for the SSO are statistical and do not include systematic errors. Panels (a)–(e) are the QFTs for  $|\psi_1\rangle$ ,  $|\psi_2\rangle$ ,  $|\psi_3\rangle$ ,  $|\psi_4\rangle$ , and  $|\psi_8\rangle$ , respectively.

11. M. D. Barrett *et al.*, "Deterministic quantum teleportation of atomic qubits," *Nature* **429**, 737–739 (2004).
12. T. Schaetz *et al.*, "Quantum Dense Coding with Atomic Qubits," *Phys. Rev. Lett.* **93**, 040505 (2004).
13. C. Monroe *et al.*, "Resolved-sideband Raman cooling of a bound atom to the 3D zero-point energy," *Phys. Rev. Lett.* **75**, 4011 (1995).
14. D. J. Wineland *et al.*, "Quantum information processing with trapped ions," *Phil. Trans. R. Soc. Lond. A* **361**, 1349–1361 (2003).
15. D. Leibfried *et al.*, "Toward Heisenberg-Limited Spectroscopy with Multiparticle Entangled States," *Science* **304**, 1476–1478 (2004).
16. W. Paul, "Electromagnetic traps for charged and neutral particles," *Rev. Mod. Phys.* **62**, 531–540 (1990).
17. P. K. Ghosh, *Ion Traps* (Clarendon Press, Oxford, 1995).
18. M. A. Rowe *et al.*, "Transport of quantum states and separation of ions in a dual rf ion trap," *Quant. Inf. Comput.* **2**, 257–271 (2002).
19. J. Preskill, "Reliable Quantum Computers," *Proc. R. Soc. Lond. A* **454**, 385–410 (1998).
20. A. R. Calderbank and P. W. Shor, "Good Quantum Error-correcting Codes Exist," *Phys. Rev. A* **54**, 1098–1105 (1996).
21. A. Steane, "Multiple Particle Interference and Quantum Error Correction," *Proc. R. Soc. Lond. A* **452**, 2551–2577 (1996).
22. D. G. Cory *et al.*, "Experimental Quantum Error Correction," *Phys. Rev. Lett.* **81**, 2152–2155 (1998).
23. D. Leung *et al.*, "Experimental Realization of a two-bit phase damping quantum code," *Phys. Rev. A* **60**, 1924–1943 (1999).
24. E. Knill, R. Laflamme, R. Martinez, and C. Negrevergne, "Benchmarking Quantum Computers: The Five-Qubit Error Correcting Code," *Phys. Rev. Lett.* **86**, 5811–5814 (2001).
25. D. G. Cory *et al.*, "NMR Based Quantum Information Processing: Achievements and Prospects," *Fortschr. Phys.* **48**, 875–907 (2000).
26. J. Chiaverini *et al.*, "Realization of quantum error correction," *Nature* **432**, 602–605 (2004).
27. M. A. Nielsen and I. L. Chuang, *Quantum Computation and Quantum Information*. Cambridge University Press, Cambridge, UK (2000).
28. B. E. King *et al.*, "Cooling the collective motion of trapped ions to initialize a quantum register," *Phys. Rev. Lett.* **81**, 1525–1528 (1998).
29. D. Coppersmith, "An Approximate Fourier Transform Useful in Quantum Factoring," IBM Research Report RC19642 (1994).
30. A. Ekert, R. Jozsa, "Quantum computation and Shor's factoring algorithm," *Rev. Mod. Phys.* **68**, 733 (1996).
31. R. B. Griffiths and C.-S. Niu, "Semiclassical Fourier transform for quantum computation," *Phys. Rev. Lett.* **76**, 3228 (1996).
32. L. M. K. Vandersypen *et al.*, "Experimental realization of an order-finding algorithm with an NMR quantum computer," *Phys. Rev. Lett.* **85**, 5452 (2000).
33. Y. S. Weinstein, M. A. Pravia, E. M. Fortunato, S. Lloyd, and D. G. Cory, "Implementation of the quantum Fourier transform," *Phys. Rev. Lett.* **86**, 1889 (2001).
34. L. M. K. Vandersypen *et al.*, "Experimental realization of Shor's quantum factoring algorithm using nuclear magnetic resonance," *Nature* **414**, 883 (2001).
35. J.-S. Lee, J. Kim, Y. Cheong, and S. Lee, "Implementation of phase estimation and quantum counting algorithms on an NMR quantum-information processor," *Phys. Rev. A* **66**, 042316 (2002).
36. Y. S. Weinstein *et al.*, "Quantum process tomography of the quantum Fourier transform," *J. Chem. Phys.* **121**, 6117 (2004).
37. J. Chiaverini *et al.*, "Implementation of the semiclassical quantum Fourier transform in a scalable system," *Science*, in press.
38. G. Arfken, *Mathematical Methods for Physicists* (Academic Press, Orlando, FL, ed. 3, 1985).
39. E. L. Hahn, "Spin echoes," *Phys. Rev.* **80**, 580 (1950).
40. L. Allen and J. H. Eberly, *Optical resonance and two-level atoms* (Dover, New York, 1987).
41. C. A. Fuchs, PhD thesis, The University of New Mexico, Albuquerque, NM (1996). arXiv e-print quant-ph/9601020.